The mysterious long-range transport of giant mineral dust particles

Michèlle van der Does[1]*, Peter Knippertz[2], Philipp Zschenderlein[2], R. Giles Harrison[3], Jan-Berend W. Stuut[1,4]

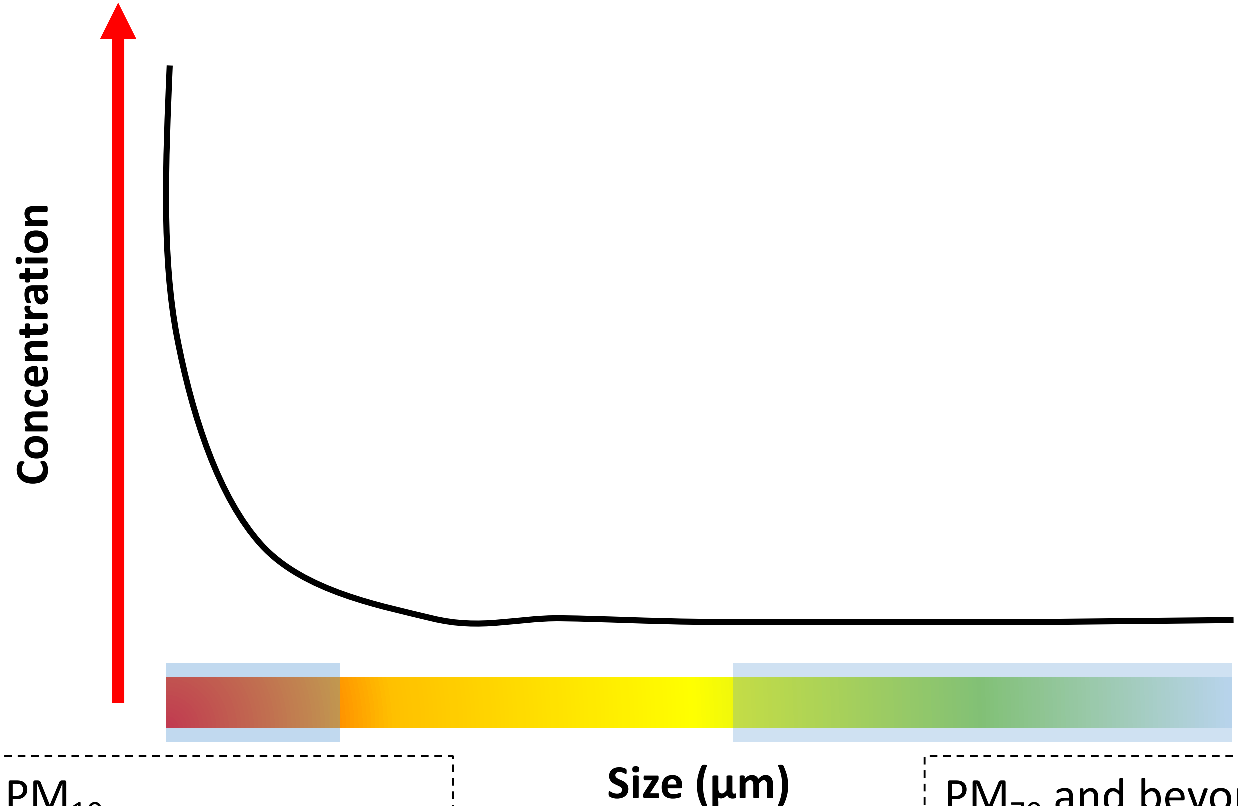

$PM_{2.5}$ and PM_{10}

Health effects
Visibility
Acid rains, soil nutrition
Prime factor in determining quality of air.

Protection via masks, filters etc.

PM_{70} and beyond

Primary concern towards environment

Global warming, radiative heating

cloud nucleation!

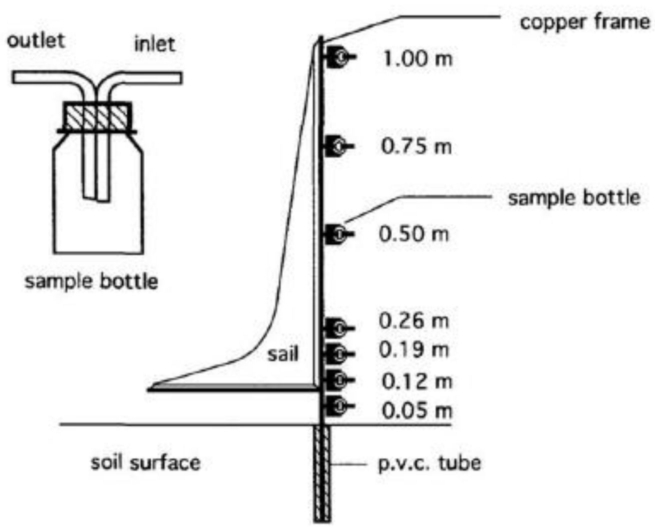

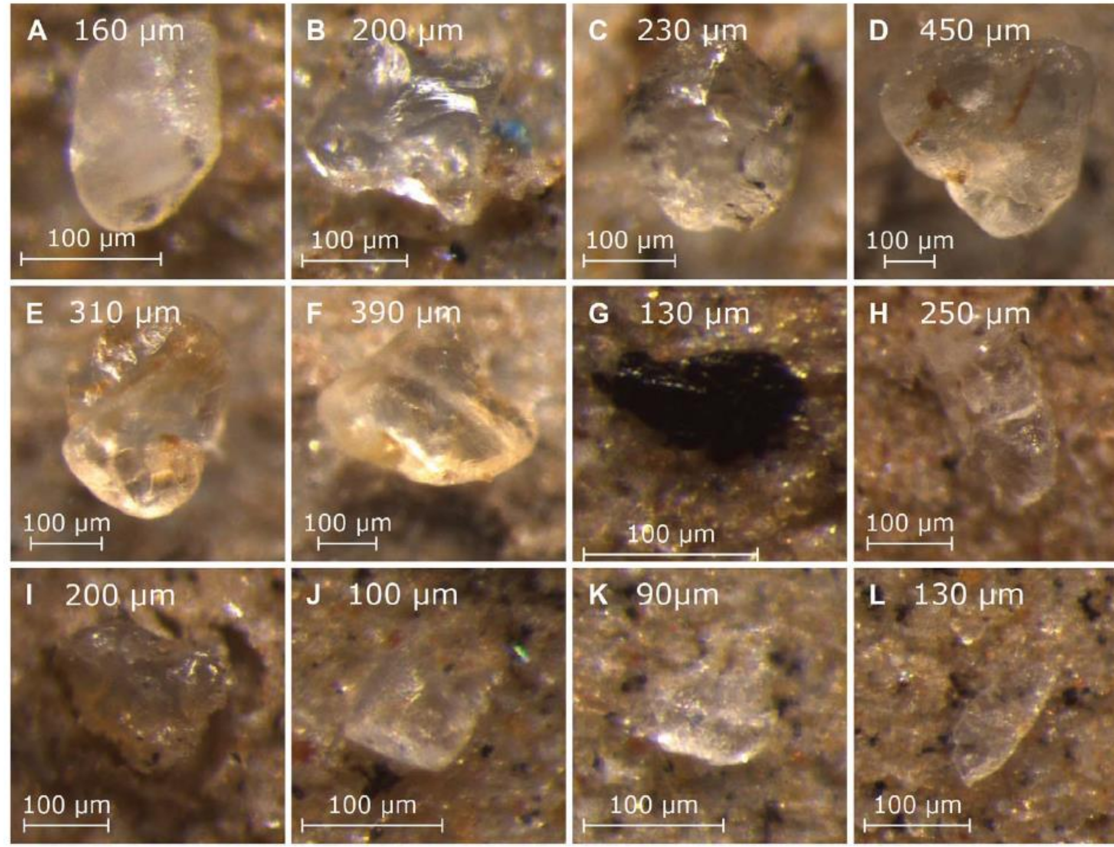

Figure: Giant mineral dust particles sampled by the MWAC samplers at M3 (12°N, 38°W) and M4 (12°N, 49°W) in 2014 and 2015, with their approximate diameters. (A to C) 2014-M3; (D to F) 2014-M4; (G to I) 2015-M3; (J to L) 2015-M4.

https://www.researchgate.net/publication/40217123_Measurement_and_analysis_methods_for_field-scale_wind_erosion_studies/figures?lo=1

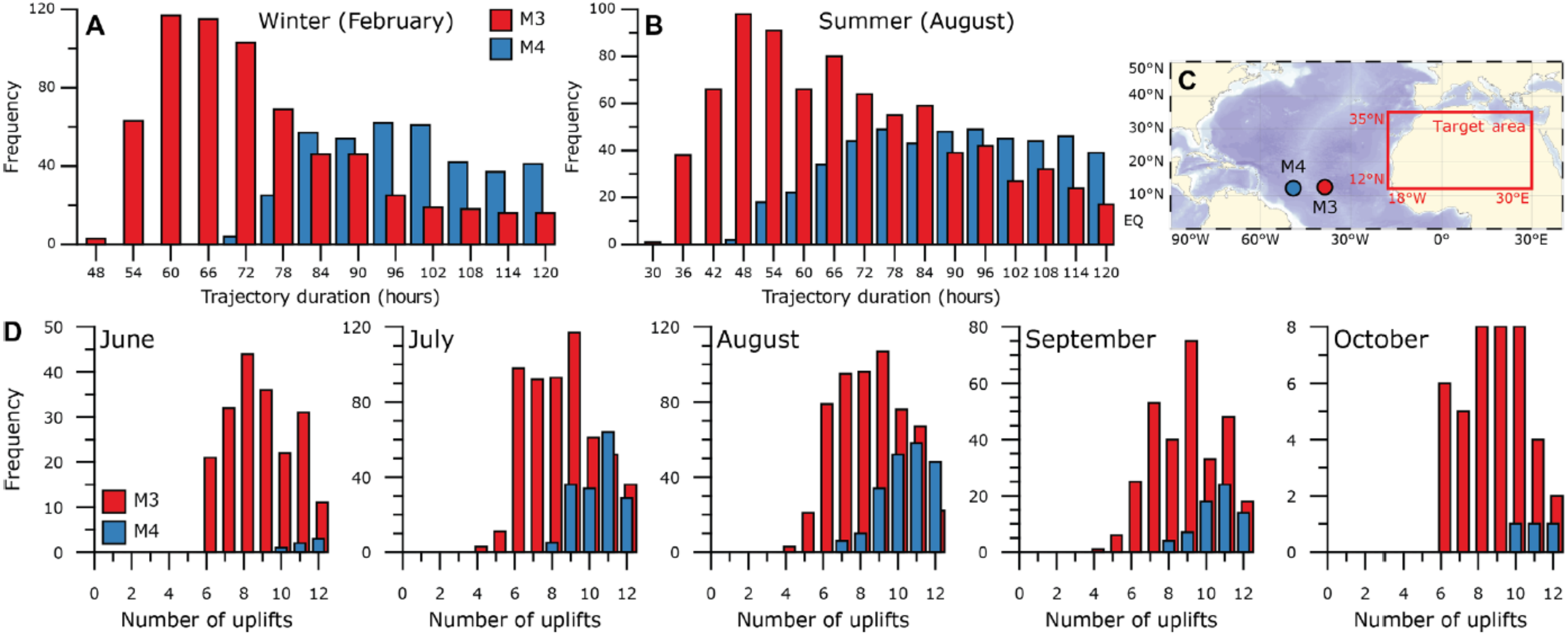

Fig. 2. Seasonality of atmospheric transport from Africa to the buoy sites. Distribution of travel times for backward trajectories from buoys M3 (red) and M4 (blue) to the target area (**C**), for February (**A**) and August (**B**). (**D**) Frequency of the minimum number of deep convective uplift cycles needed for a 100-μm particle to travel from the target area (C) to the sampling buoys M3 (red) and M4 (blue), assuming a constant sedimentation velocity of 400 mm s^{-1} (Table 2), for June to October. All computations are based on ERA-Interim data during the 10-year period 2006 to 2015.

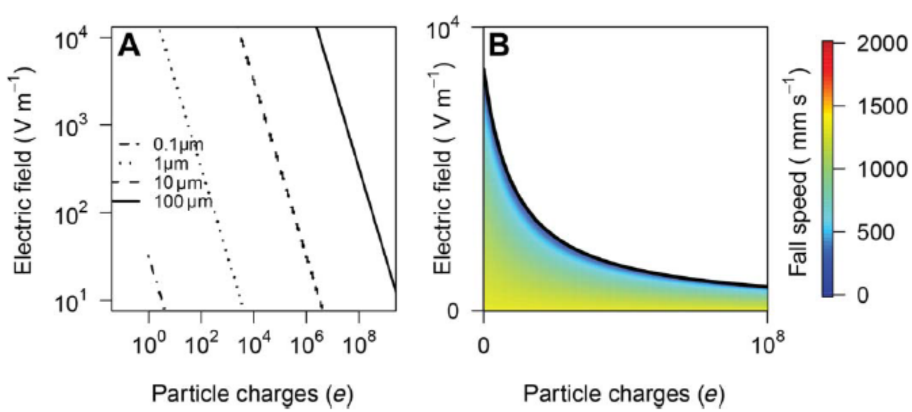

Fig. 3. Influence of charge and electric field on the net force on a particle. (**A**) Combination of particle charge and local electric field required for the magnitude of the electric force experienced by a particle to equal the particle's weight, for particles having diameters of 0.1, 1, 10, and 100 μm. (**B**) Fall speed for a 100-μm quartz particle for increasing electric field and particle charge (density of quartz = 2648 kg m^{-3}, drag coefficient C_D = 1.5).

Table 1. Sampling duration of MWAC samplers on the dust-collecting buoys at M3 and M4 (Fig. 2), together with statistics on the colocated wind measurements.

	Sampling start	Sampling end	Days sampled	Minimum wind velocity (m s^{-1})	Maximum wind velocity (m s^{-1})	Average wind velocity (m s^{-1})
2014-M3	24 November 2013	01 September 2014	281	1.9	13.6	8.7 ± 2.0
2014-M4	28 November 2013	27 January 2015	425	4.5	14.2	9.1 ± 1.8
2015-M3	22 November 2015	29 March 2016	432	0.9	12.7	6.7 ± 1.7

Table 2. Settling velocities after Bagnold (*19*) and estimates of traveled distance based on favorable summer (strong winds and elevated dust) and winter (lower wind speeds and elevation) conditions.

Particle size (μm)	Settling velocity (mm s^{-1})	Summer: Traveled distance at 25 m s^{-1} winds from 7-km altitude	Winter: Traveled distance at 10 m s^{-1} winds from 3-km altitude
100	400	438 km	75 km
200	1000	175 km	30 km
300	1500	117 km	20 km

Conclusion:

- Strong winds causing fast horizontal transport greatly enhance the distance over which the dust travels
- Transport of individual large dust particles is further aided by strong turbulence, keeping them in suspension for a longer time
- Particle charge affects their dynamics and, for negatively charged particles, can offset a particle's weight in a downward directed electric field, so keeping it aloft for longer
- Thunderstorms or tropical cyclones can carry dust particles to great heights, strongly increasing their horizontal travel distance if the particles can leave the storm through the anvil or upper-level outflow region without being rained out.

High Efficiency, Transparent, Reusable, and Active PM2.5 Filters by Hierarchical Ag Nanowire Percolation Network

Seongmin Jeong,[†] Hyunmin Cho,[†] Seonggeun Han,[†] Phillip Won,[†] Habeom Lee,[†] Sukjoon Hong,[‡] Junyeob Yeo,[§] Jinhyeong Kwon,[*,†] and Seung

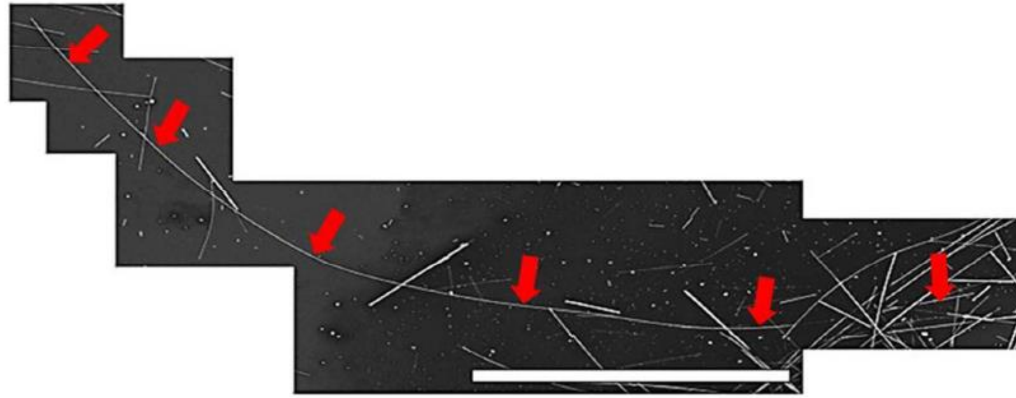

Cryst. Growth Des. 2012, 12, 5598−5605

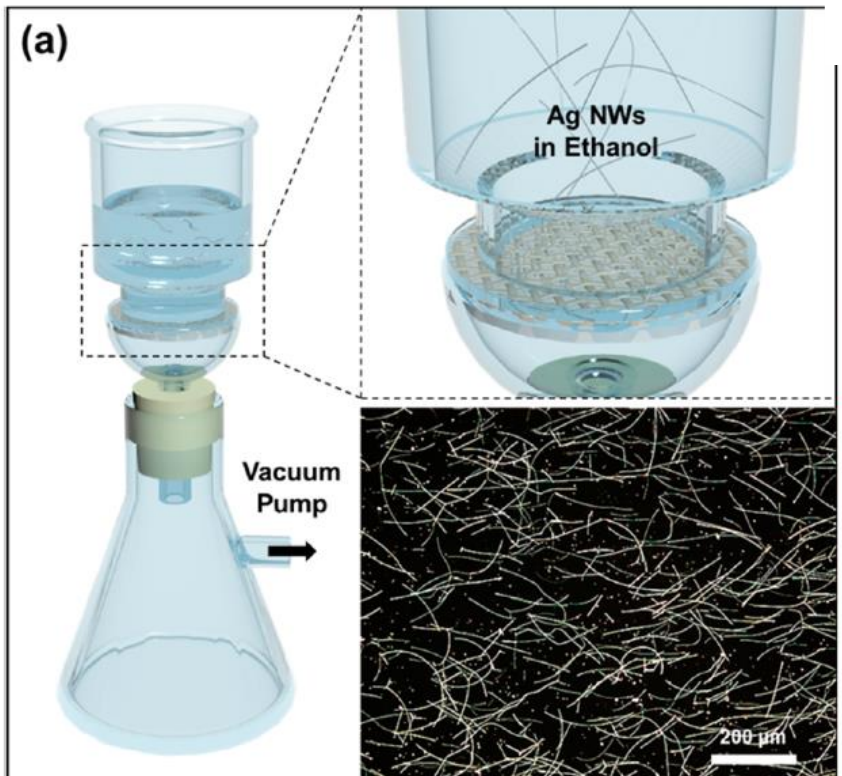

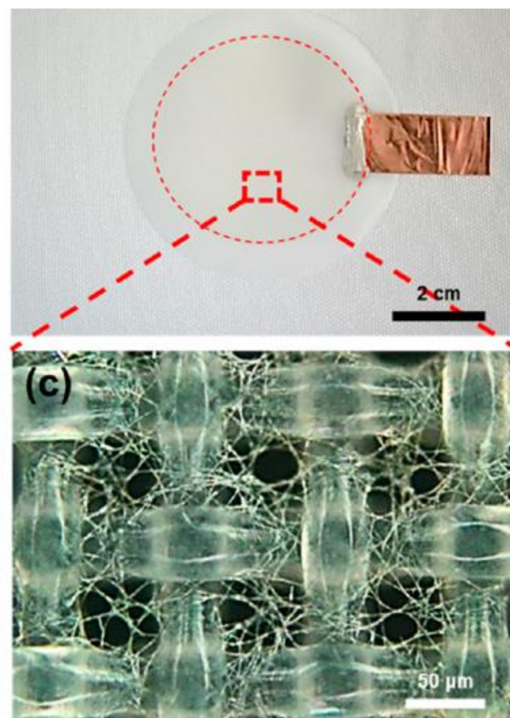

DOI: 10.1021/acs.nanolett.7b01404
Nano Lett. 2017, 17, 4339−4346

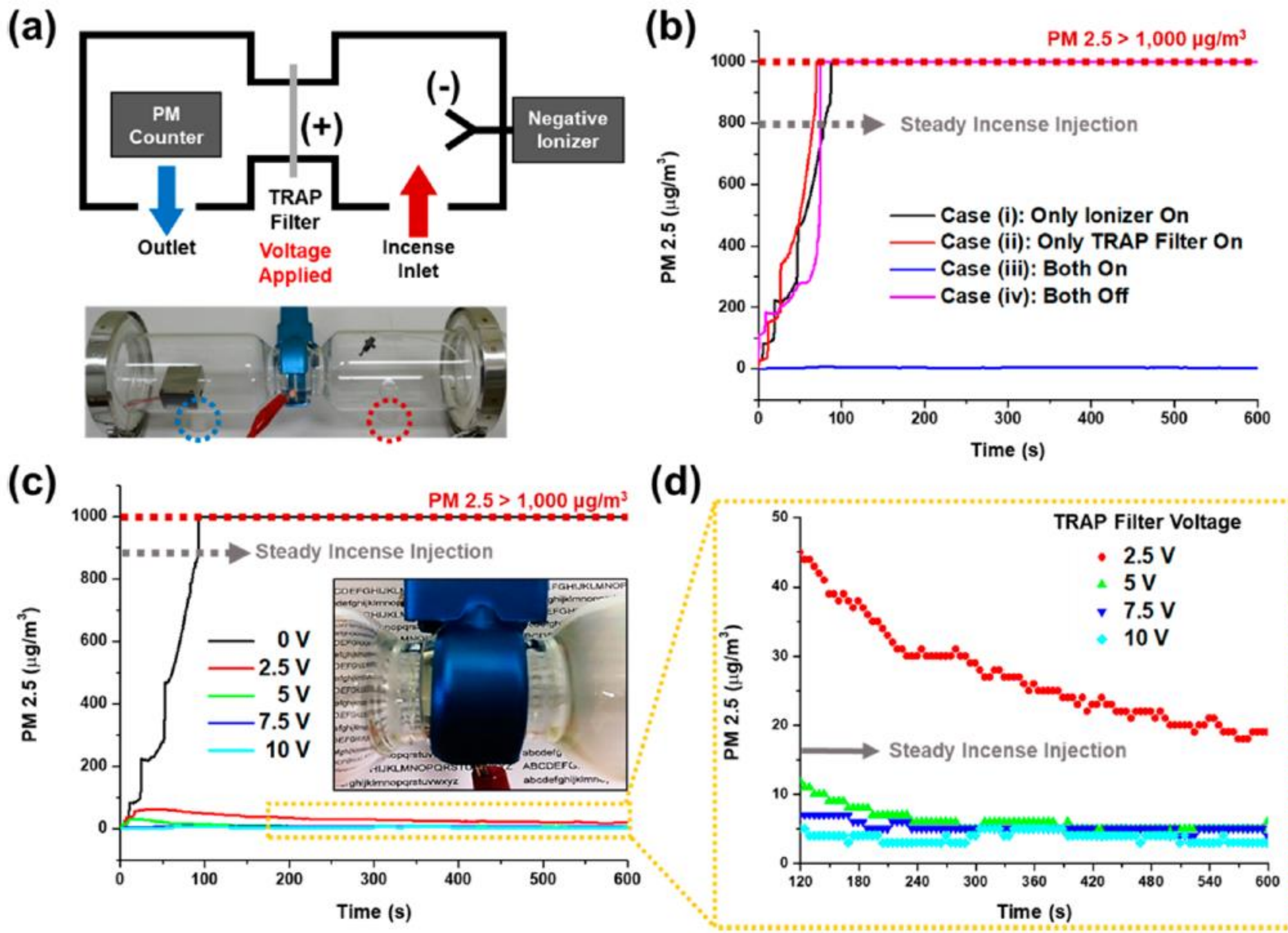

Figure 2. (a) Schematic (top) and digital camera image (bottom) of TRAP filter experimental setup. The PM counter sensor is placed in the left side of the chamber, while the PM is generated from incense at the right side of the chamber. TRAP filter is sandwiched between the two chambers. (b) Transient evolution of PM2.5 removal performance for (i) only ionizer on (5 V), (ii) only TRAP filter on (10 V), (iii) both trap filter and ionizer on, and (iv) both off. The PM density showed saturation at 1000 $\mu g/m^3$ due to detector limit. (c) Transient evolution of PM2.5 density for various TRAP filter voltage condition. (d) Magnified view of graph (c) after 120 s from the PM detection for various TRAP filter voltage conditions.

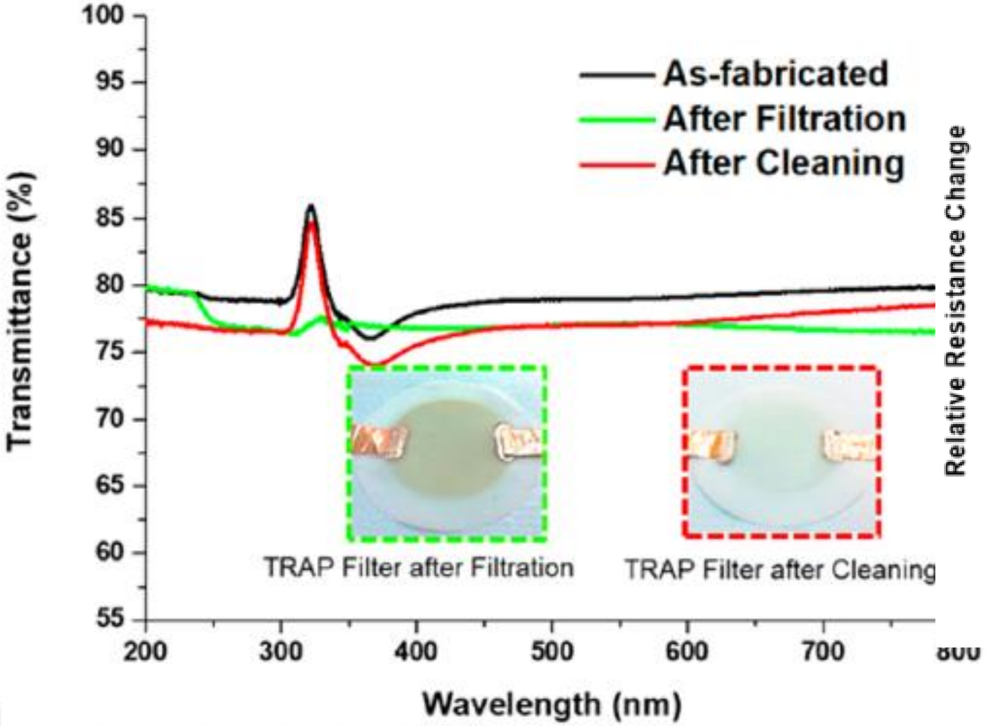
As-fabricated
After Filtration
After Cleaning
TRAP Filter after Filtration
TRAP Filter after Cleaning
Transmittance (%)
Wavelength (nm)
100
95
90
85
80
75
70
65
60
55
200
300
400
500
600
700
800

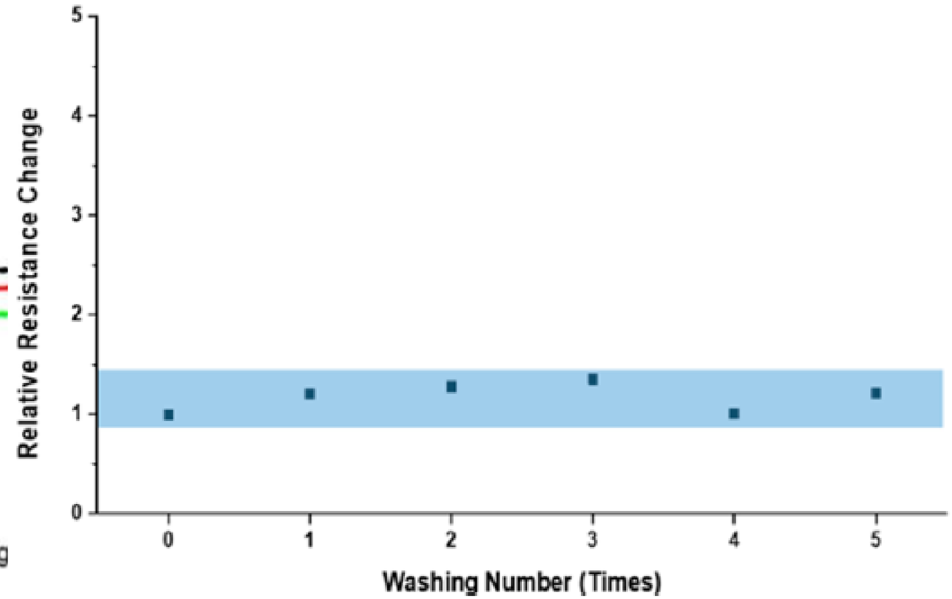
Relative Resistance Change
Washing Number (Times)
0
1
2
3
4
5

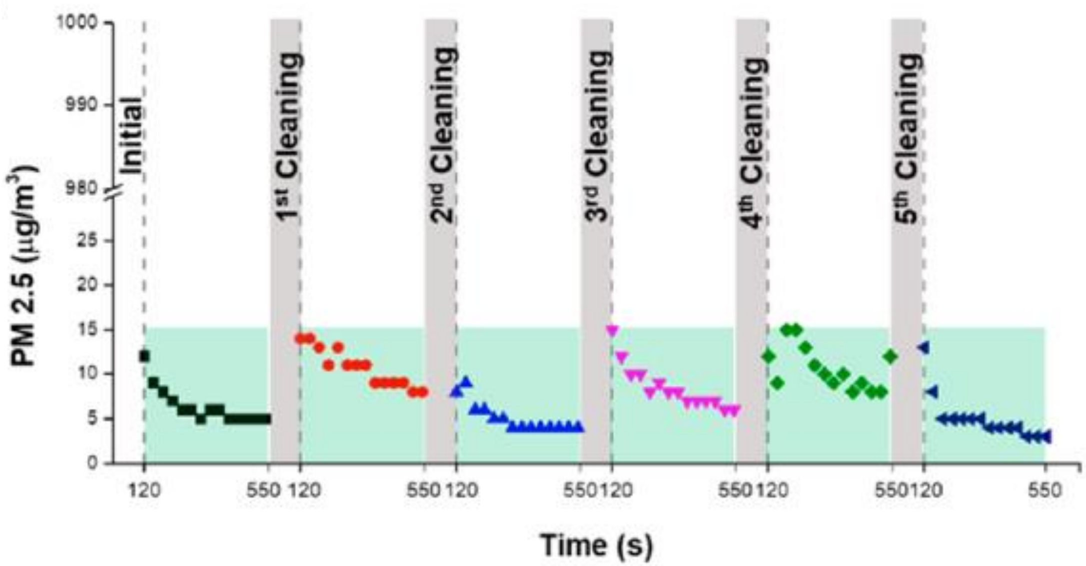
Initial
1st Cleaning
2nd Cleaning
3rd Cleaning
4th Cleaning
5th Cleaning
PM 2.5 (μg/m3)
Time (s)
1000
990
980
25
20
15
10
5
0
120
550

Conclusion:

- First environmental application demonstration of Ag nanowire percolation network

- Electrical type of PM2.5 filter that is transparent, reusable, and active using a highly conductive and transparent Ag nanowire percolation network electrode

- Compared with previous PM filter study using short-range intermolecular force in polar polymeric nanofiber, the TRAP filter uses both long-range electrostatic force and short-range van der Waals force when low voltage is applied on the metal nanowire network

nature COMMUNICATIONS

Metal-organic frameworks with photocatalytic bactericidal activity for integrated air cleaning

Ping Li[1], Jiazhen Li[1], Xiao Feng[1], Jie Li[1], Yuchen Hao[1], Jinwei Zhang[1], Hang Wang[1], Anxiang Yin[1], Junwen Zhou[1], Xiaojie Ma[1] & Bo Wang[1]

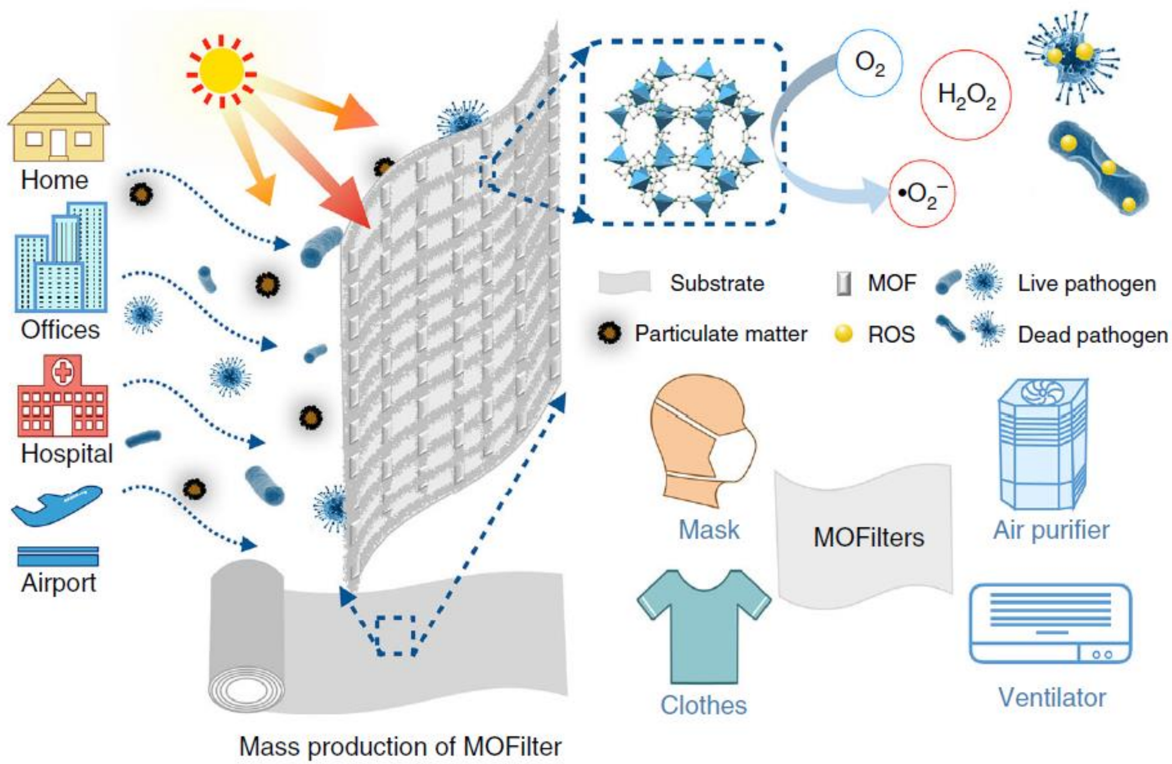

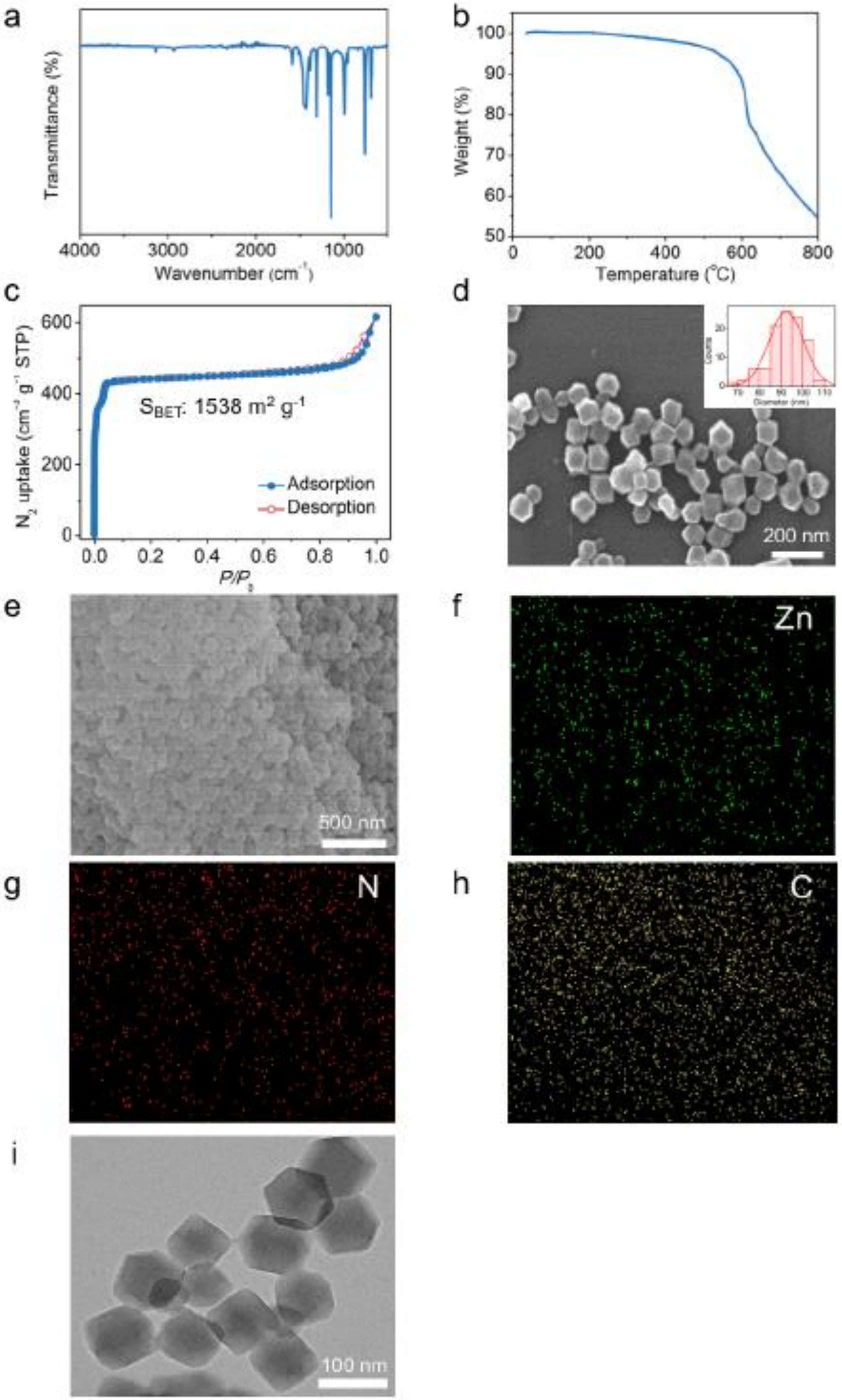

Supplementary Figure 2 **a** FT-IR spectra, **b** TG curve, **c** N_2 sorption isotherms measured at 77 K, **d** SEM image and size distribution (insert), **e-h** elemental mapping analysis, **i** TEM image of ZIF-8.

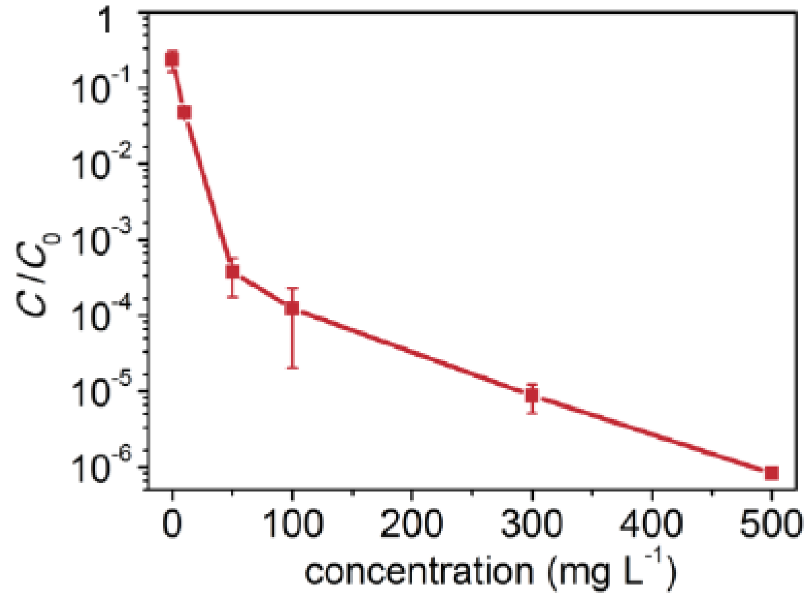

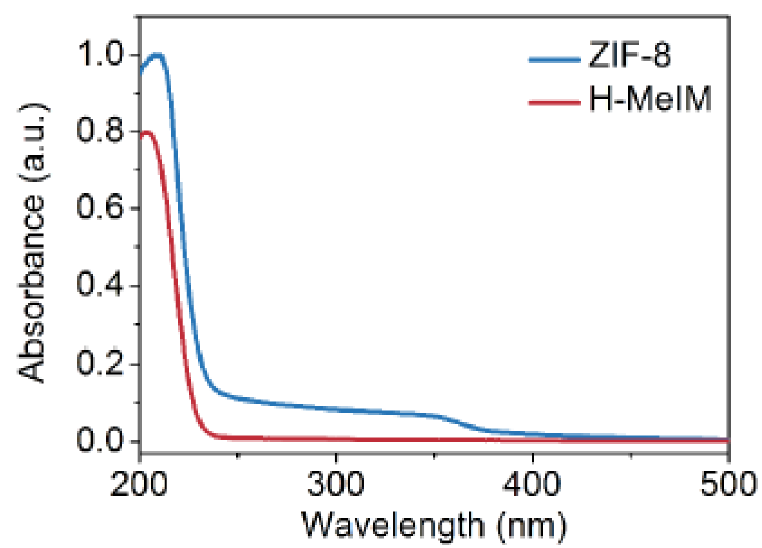

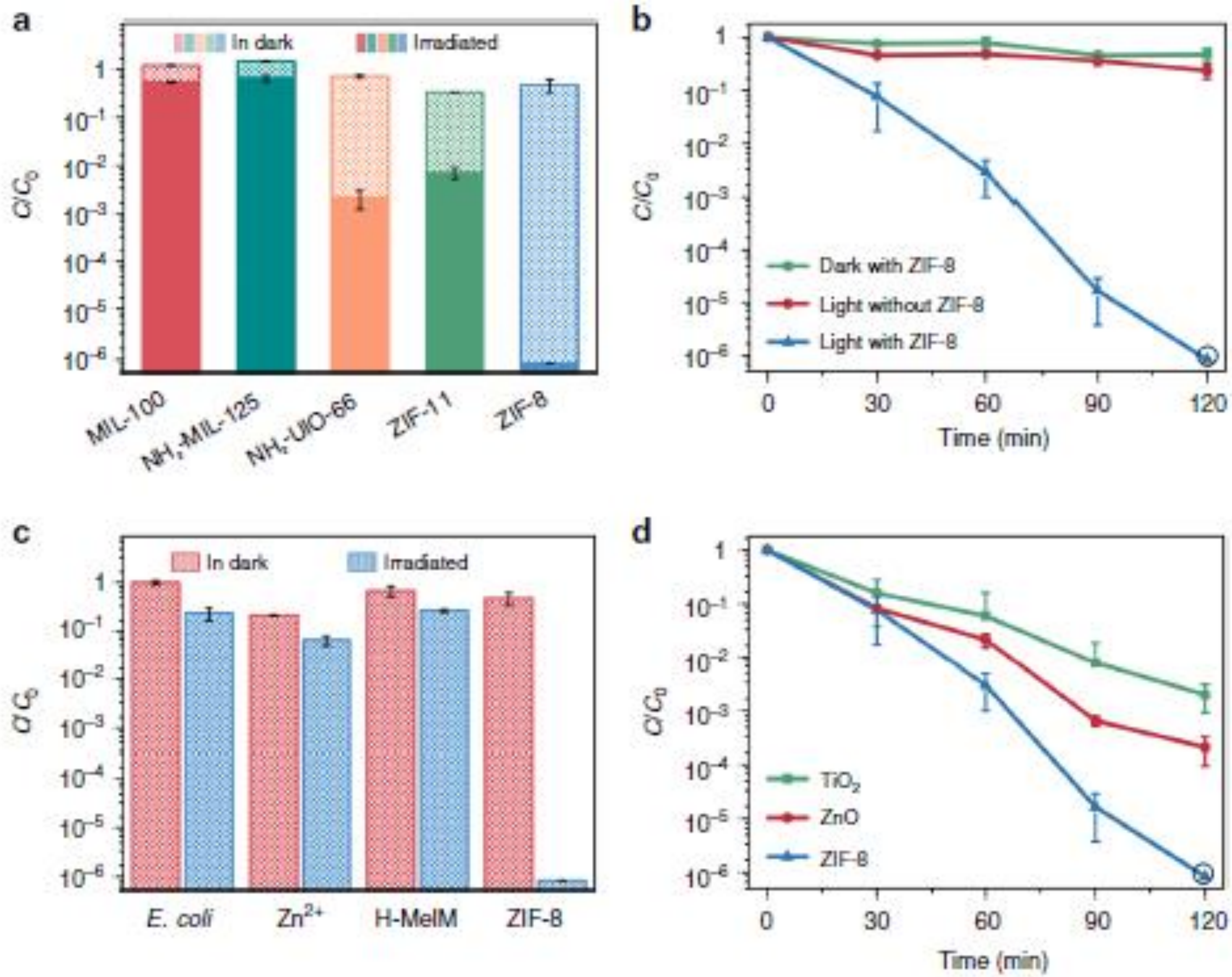

Fig. 2 Photocatalytic disinfection performance of ZIF-8 (zinc-imidazolate MOF). **a** Disinfection performance comparison among five metal-organic frameworks (MOFs). **b** Inactivation kinetics of *E. coli* in the presence of ZIF-8. **c** Inactivation efficiency against *E. coli* in the presence of Zn^{2+} (3 mg L^{-1}), 2-methylimidazole (H-MeIM) (7 mg L^{-1}), and ZIF-8 (500 mg L^{-1}), respectively. **d** Disinfection performance comparison among ZIF-8, TiO_2, and ZnO under simulated solar irradiation. In the disinfection performance, the error bars are calculated via repeating the measurements for three times and the black circle represents no measurable levels of bacteria in the culture medium

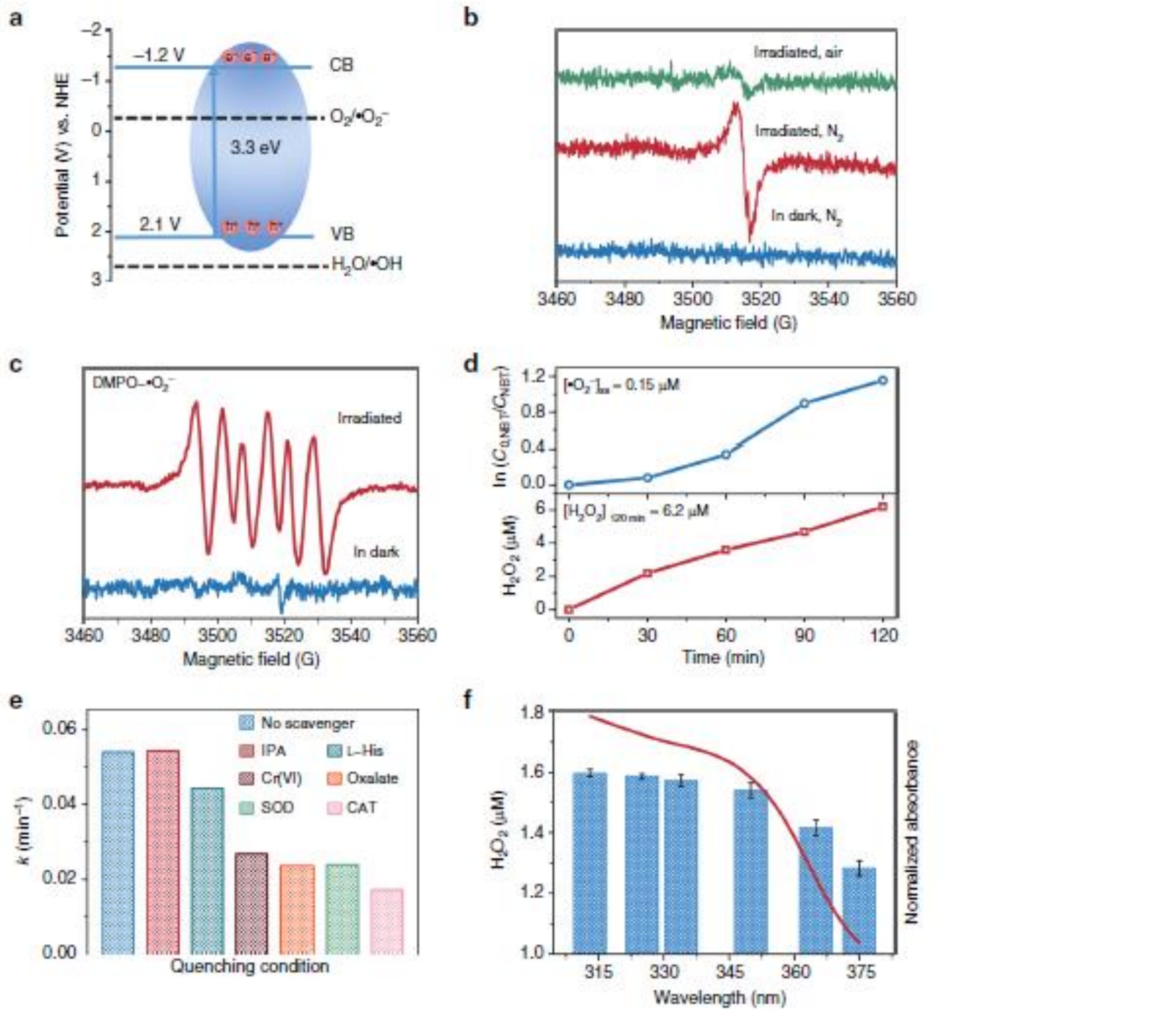

Fig. 3 Band-structure characterization and photocatalytic disinfection mechanism of ZIF-8 (zinc-imidazolate MOF). **a** The band positions of ZIF-8 with respect to the reactive oxygen species (ROS) formation potential. Conduction band (CB) and valence band (VB) represent conduction band and valence band respectively. **b** Electron paramagnetic resonance (EPR) spectra of ZIF-8 at 77 K in dark and under light irradiation (300 nm < λ < 1100 nm) in different atmosphere. **c** EPR spectra of DMPO−$•O_2^-$ for ZIF-8 under light irradiation and in dark. **d** Steady-state concentration of $•O_2^-$ calculated from the decay of nitroblue tetrazolium (NBT) and hydrogen peroxide (H_2O_2) accumulation over time, respectively. **e** The first-order disinfection rate on ZIF-8 with different scavengers (IPA → $•OH$, L-His → $^1O_2$, Cr(VI) → e^-, Oxalate → h^+, SOD → $•O_2^-$, CAT → H_2O_2). **f** Dependence of the amount of released H_2O_2 by ZIF-8 on the wavelength of incident light and the ultraviolet-visible (UV-vis) spectra of ZIF-8. The error bars are calculated via repeating the measurements for three times. SOD superoxide dismutase, IPA isopropanol, DMPO 5,5-diemthyl-1-pyrroline N-oxide

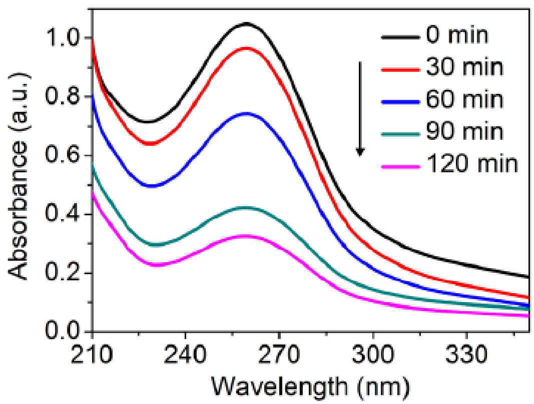

Supplementary Figure 13. Time-dependent absorption spectra of nitroblue tetrazolium (NBT) for $\bullet O_2^-$ detection

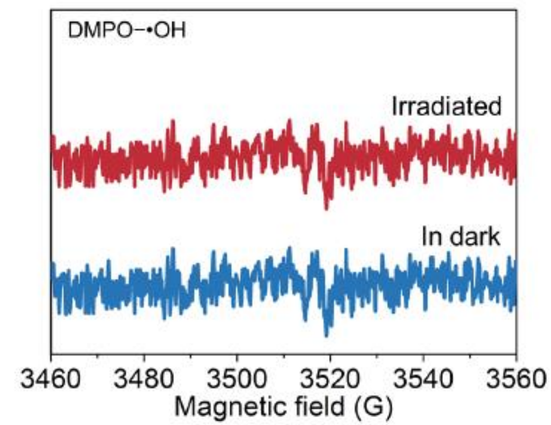

Supplementary Figure 14. EPR spectra of DMPO−•OH recorded in ZIF-8 aqueous solution suspension under light and dark conditions.

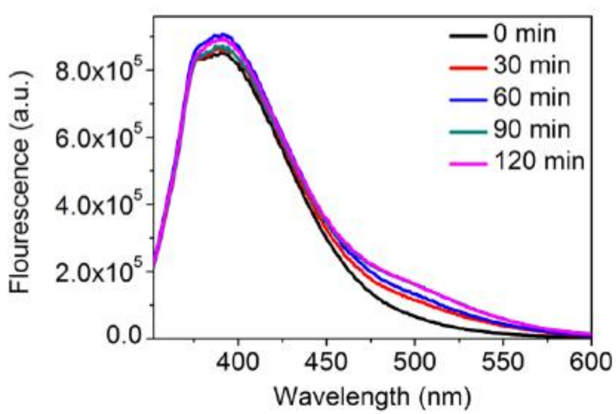

Supplementary Figure 15. Time-dependent fluorescence spectra of generated 7-hydroxycoumarin in ZIF-8 reaction system for •OH detection. 7-hydroxycoumarin could emit fluorescence at 455 nm when excited at 332 nm.

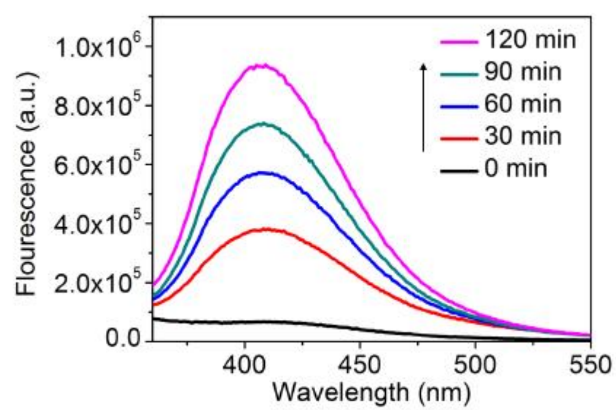

Supplementary Figure 16. Time-dependent fluorescence spectra of produced p-hydroxyphenylacetic acid dimer in reaction system for H_2O_2 detection.

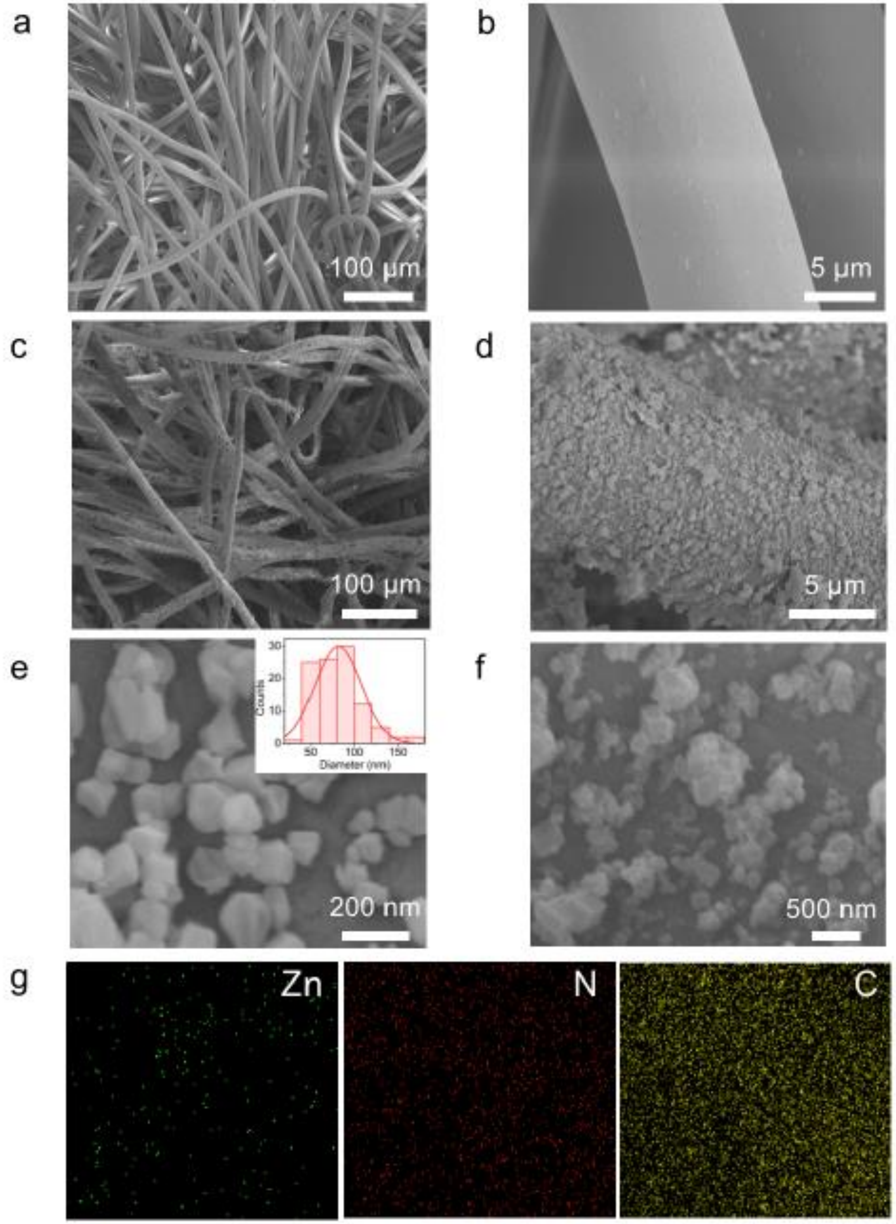

Supplementary Figure 20. a, b SEM images of NWF, **c, d, e** SEM images of MOFilter and size distribution of ZIF-8 particles grown on fibers (insert), **f, g** corresponding elemental mapping images.

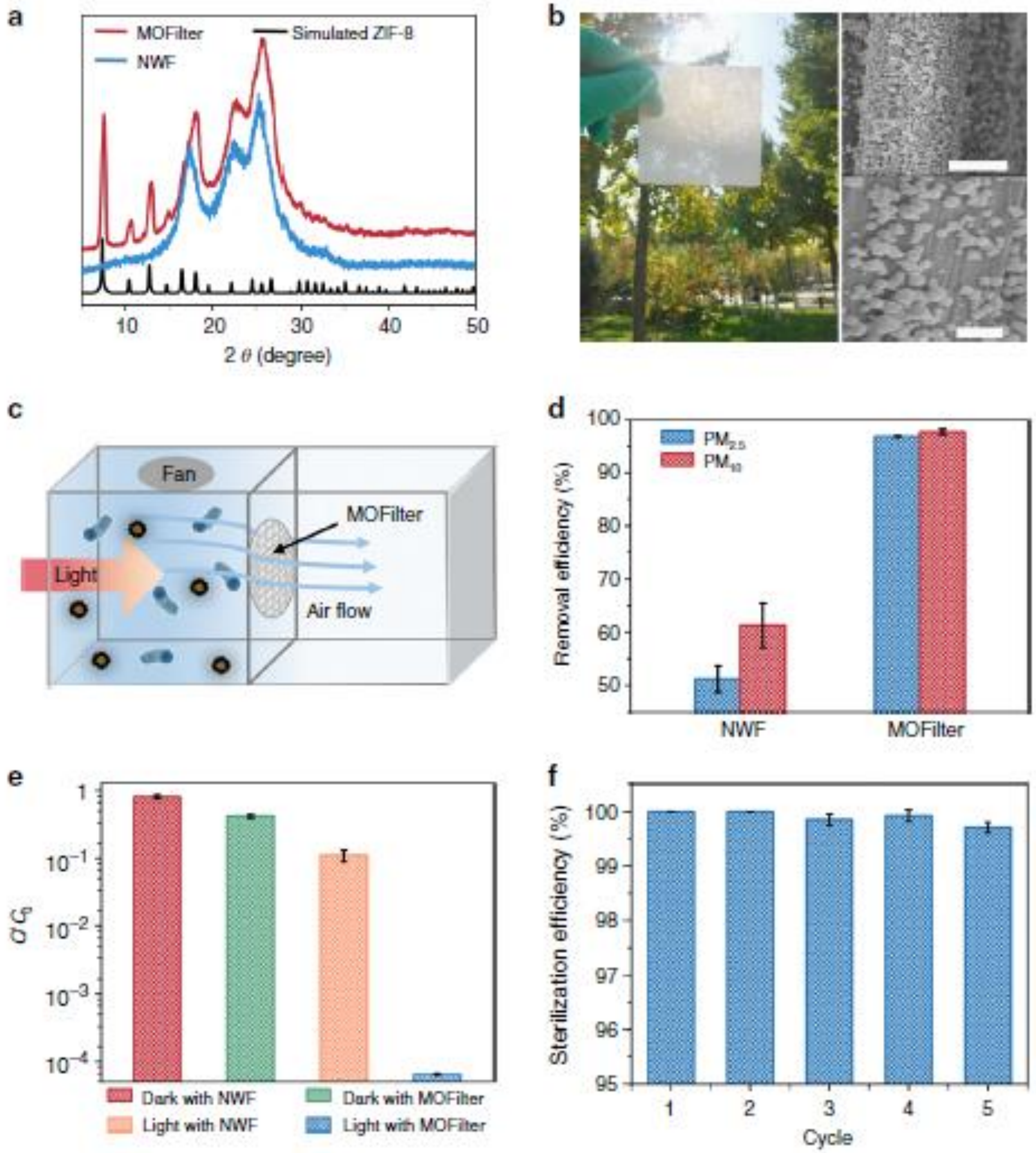

Fig. 4 Characterization of metal-organic framework (MOF)-based filter (MOFilter) and its air cleaning performance. **a** X-ray diffraction (XRD) patterns of non-woven fabric (NWF) and MOFilter. **b** Optical photo and scanning electron microscopy (SEM) images of MOFilter (scale bar, 5 μm (top); 1 μm (bottom)). **c** Schematic representation of the air cleaning system. **d** Comparison of the particulate matter (PM) filtration efficiency between MOFilter and NWF. **e** Comparison of the air disinfection performance between MOFilter and NWF under light and dark conditions, respectively. **f** Air disinfection performance of MOFiter continuously used for five cycles. The error bars are calculated via repeating the measurements for three times

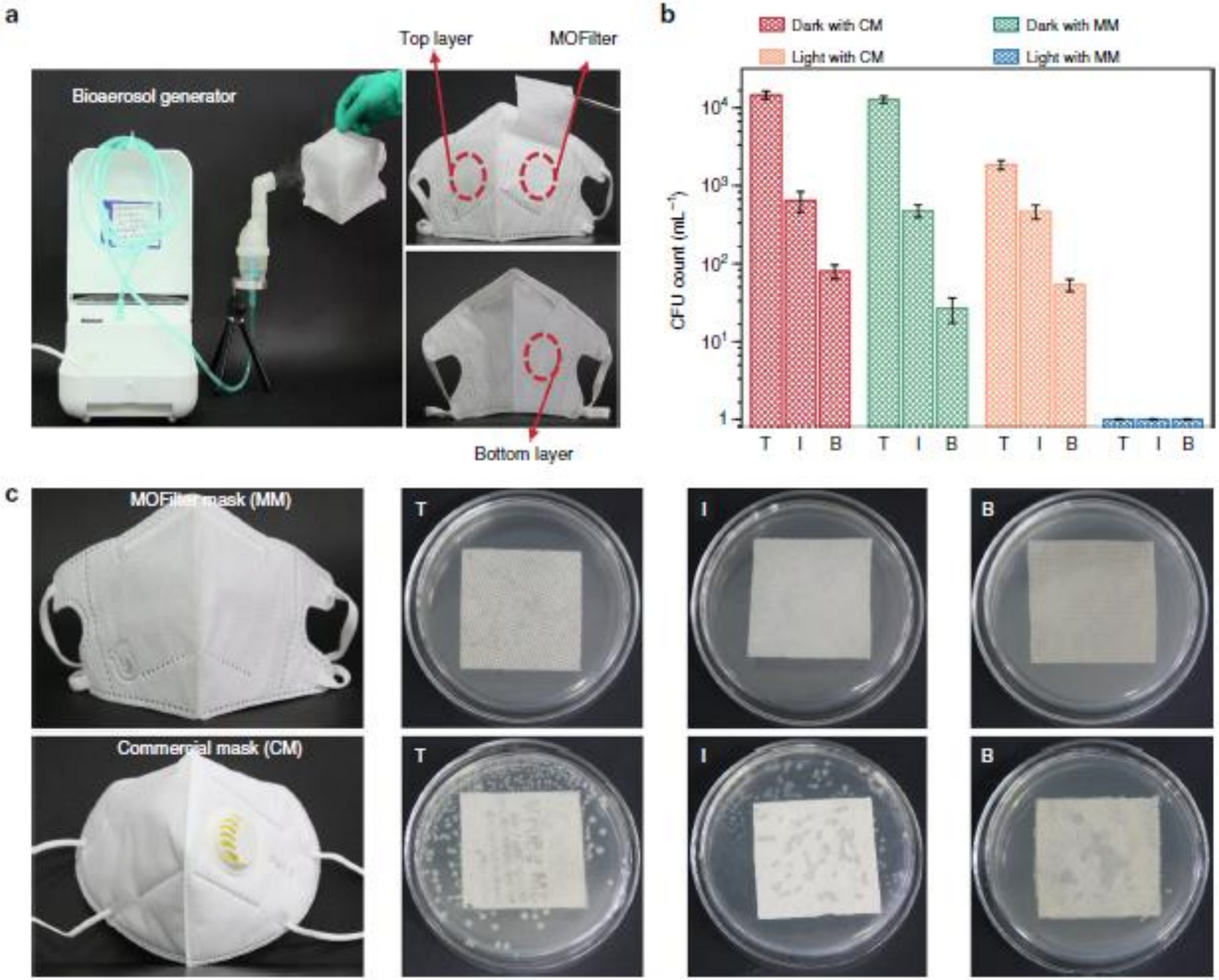

Fig. 5 Antibacterial performance comparison between metal-organic framework (MOF)-based filter (MOFilter) mask (MM) and commercial mask (CM). **a** Bioaerosol generation apparatus and optical images of trilaminar MOFilter mask. **b**, **c** *Escherichia coli* levels residual on top, inner and bottom layers of MM and CM, respectively, after 30 min of light irradiation. The number of viable cells in **b** is determined from saline eluent used for collecting living bacteria on each layer of mask after reaction. The bacterial colonies residual on eluent-treated mask are shown in **c**. The top, inner, and bottom layers are denoted as T, I and B, respectively. The error bars are calculated via repeating the measurements for three times

Conclusion:

- Photocatalytic disinfection activity of ZIF-8 and its potential use in air purification was explored
- The charge-trapping centers Zn+ can be photogenerated on MOF surface via LMCT, and effectively active O_2 to form $\bullet O_2^-$ and related ROS like H_2O_2
- Furthermore, ZIF-8 is processed as filters with the combination of PM filtration and bacteria-killing function
- ZIF-8-based filter could offer strong and comprehensive protection against air hazards including PM and pathogens aerosols